Reversible CO Binding Enables Tunable CO/H-2 and CO/N-2 Separations in Metal-Organic Frameworks with Exposed Divalent Metal Cations

(Article begins on next page)

07 August 2024

by

Eric D. Bloch, Matthew R. Hudson, Jarad A. Mason, Sachin Chavan, Valentina Crocellà, Joshua D. Howe, Kyuho Lee, Allison L. Dzubak, Wendy L. Queen, Joseph M. Zadrozny, Stephen J. Geier, Li-Chiang Lin, Laura Gagliardi, Berend Smit, Jeffrey B. Neaton, Silvia Bordiga, Craig M. Brown, and Jeffrey R. Long

Reversible CO Binding Enables Tunable CO/H$_2$ and CO/N$_2$ Separations in Metal–Organic Frameworks with Exposed Divalent Metal Cations

Eric D. Bloch†, Matthew R. Hudson‡, Jarad A. Mason†, Sachin Chavan§, Valentina Crocellà§, Joshua D. Howe‖⊥, Kyuho Lee‖⊥, Allison L. Dzubak#, Wendy L. Queen‡⊥, Joseph M. Zadrozny†, Stephen J. Geier†, Li-Chiang Lin‖, Laura Gagliardi#, Berend Smit†‖¶, Jeffrey B. Neaton⊥¶○□, Silvia Bordiga§, Craig M. Brown‡∇, and Jeffrey R. Long*†¶

† Department of Chemistry, University of California, Berkeley, California 94720, United States

‡ Center for Neutron Research, National Institute of Standards and Technology, Gaithersburg, Maryland 20899, United States

§ Department of Chemistry, NIS and INSTM Centre of Reference, University of Turin, Via Quarello 15, I-10135 Torino, Italy

‖ Department of Chemical and Biomolecular Engineering, University of California, Berkeley, California 94720, United States

⊥ The Molecular Foundry, Lawrence Berkeley National Laboratory, Berkeley, California 94720, United States

Department of Chemistry, Chemical Theory Center, and Supercomputing Institute, University of Minnesota, Minneapolis, Minnesota 55455, United States

∇ Department of Chemical Engineering, University of Delaware, Newark, Delaware 19716, United States

¶ Materials Sciences Division, Lawrence Berkeley National Laboratory, Berkeley, California 94720, United States

○ Department of Physics, University of California, Berkeley, Berkeley, California 94720, United States

□ Kavli Energy NanoSciences Institute at Berkeley, Berkeley, California 94720, United States

Abstract

Six metal–organic frameworks of the M$_2$(dobdc) (M = Mg, Mn, Fe, Co, Ni, Zn; dobdc^{4-} = 2,5-dioxido-1,4-benzenedicarboxylate) structure type are demonstrated to bind carbon monoxide reversibly and at high capacity. Infrared spectra indicate that, upon coordination of CO to the divalent metal cations lining the pores within
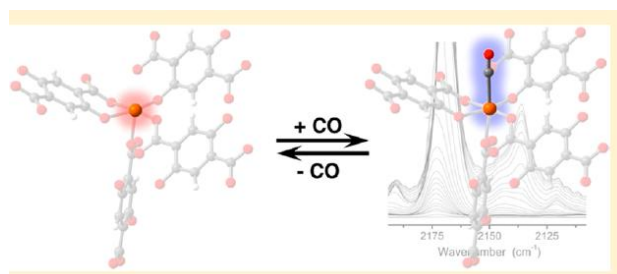
these frameworks, the C–O stretching frequency is blue-shifted, consistent with nonclassical metal-CO interactions. Structure determinations reveal M–CO distances ranging from 2.09(2) Å for M = Ni to 2.49(1) Å for M = Zn and M–C–O angles ranging from 161.2(7)° for M = Mg to 176.9(6)° for M = Fe. Electronic structure calculations employing density functional theory (DFT) resulted in good agreement with the trends apparent in the infrared spectra and crystal structures. These results represent the first crystallographically characterized magnesium and zinc carbonyl compounds and the first high-spin manganese(II), iron(II), cobalt(II), and nickel(II) carbonyl species. Adsorption isotherms indicate reversible adsorption, with capacities for the Fe, Co, and Ni frameworks approaching one CO per metal cation site at 1 bar, corresponding to loadings as high as 6.0 mmol/g and 157 cm^3/cm^3. The six frameworks display (negative) isosteric heats of CO adsorption ranging from 52.7 to 27.2 kJ/mol along the series Ni > Co > Fe > Mg > Mn > Zn, following the Irving–Williams stability order. The reversible CO binding suggests that these frameworks may be of utility for the separation of CO from various industrial gas mixtures, including CO/H$_2$ and CO/N$_2$. Selectivities determined from gas adsorption isotherm data using ideal adsorbed solution theory (IAST) over a range of gas compositions at 1 bar and 298 K indicate that all six M$_2$(dobdc) frameworks could potentially be used as solid adsorbents to replace current cryogenic distillation technologies, with the choice of M dictating adsorbent regeneration energy and the level of purity of the resulting gases.

Introduction

The coordination of carbon monoxide to transition metals has been rigorously investigated for over a century and has played an essential role in the development of our understanding of chemical bonding.[1] Since the original synthesis of Pt(CO)$_2$Cl$_2$, carbonyl complexes have been isolated and characterized for nearly every transition metal, in varying oxidation states and overall coordination numbers.[2] The vast majority of these species feature CO irreversibly bound to low-valent, low-spin transition metal centers that are able to engage in the metal-to-CO π-backbonding required for strong binding. For systems in which π-backbonding is absent or diminished, such as complexes containing d^0 or high-spin metals in higher oxidation states, carbonyl complexes remain elusive.[3] Here, we show that CO can reversibly bind to the coordinatively unsaturated M^{2+} cations lining the surfaces within the metal–organic frameworks M$_2$(dobdc) (M = Mg, Mn, Fe, Co, Ni, Zn; dobdc^{4-} = 2,5-dioxido-1,4-benzenedicarboxylate), providing the first crystallographically characterized magnesium and zinc carbonyl compounds and the first high-spin manganese(II), iron(II), cobalt(II), and nickel(II) carbonyl species. Although high-spin metals with open coordination sites typically either reject CO binding or undergo a reduction in spin upon CO coordination, the weak-field ligand dobdc^{4-} enforces a high-spin electron configuration for the M^{2+} centers in M$_2$(dobdc)[4] even in the presence of the strong-field ligand CO. Furthermore, the metal–organic framework lattice likely helps to maintain a high-spin state, as these materials would have to undergo significant structural changes to accommodate the smaller low-spin M^{2+} ions. As a result, these materials can be anticipated to display weak to moderate CO binding and complete reversibility, a property that could potentially be exploited for removing CO from various gas mixtures, enabling, for example, the energy-efficient separation of CO from H$_2$ at high capacities and various levels of purity.

Indeed, in addition to its fundamental significance, carbon monoxide has become an increasingly important chemical for the synthesis of a variety of chemical commodities, including many monomers and polymers, ethanol and other alcohols, and acetic acid. There are currently a number of competing technologies for its synthesis, the main products of which are carbon monoxide and hydrogen (syngas), typically present in H$_2$:CO ratios between 1 and 3.[5] To use carbon monoxide as a feedstock, the ratio must be reduced. Although energy-intensive cryogenic distillation is currently employed to separate these mixtures, a number of alternative methods, including membrane[6] and adsorptive separations,[7] have recently been investigated for use in the

3

production of pure carbon monoxide. Given their high density of coordinatively unsaturated metal cation sites, metal–organic frameworks of the M_2(dobdc) structure type[8] hold considerable promise for the adsorptive separation of gas streams, including mixtures of CO_2/N_2,[8f, 9] CO_2/H_2,[10] O_2/N_2,[8g] CH_4/N_2,[11] paraffins/olefins,[12] and stand poised for the separation of gas mixtures containing carbon monoxide.

Experimental Section

Sample Preparation

All reagents were obtained from commercial vendors and used without further purification. The compounds Mg_2(dobdc),[8f] Fe_2(dobdc),[8g] Mn_2(dobdc),[12c] Co_2(dobdc),[8f] Ni_2(dobdc),[8f] and Zn_2(dobdc)[8f] were synthesized according to previously published methods.

Adsorption Isotherm Fitting

Prior to fitting all CO, N_2, and H_2 adsorption isotherms, experimentally measured excess adsorption (n_{ex}) values were converted to total adsorption (n_{tot}) using eq 1, with the total pore volumes (V_p; Table S1, Supporting Information) calculated from 77 K N_2 isotherms ($P/P_0 = 0.9$) and the bulk gas density (ρ_{bulk}) at each temperature and pressure obtained from the NIST Refprop database.[13]

$$n_{tot} = n_{ex} + V_p \cdot \rho_{bulk}(P, T) \tag{1}$$

Total adsorption isotherms for each M_2(dobdc) compound were then fit with either a single-, dual-, or triple-site Langmuir equation (eq 2), where n is the total amount adsorbed in mmol/g, P is the pressure in bar, $n_{sat,i}$ is the saturation capacity in mmol/g, and b_i is the Langmuir parameter in bar^{-1} for up to three sites 1, 2 and 3.

$$n = \frac{n_{sat,1}b_1P}{1 + b_1P} + \frac{n_{sat,2}b_2P}{1 + b_2P} + \frac{n_{sat,3}b_3P}{1 + b_3P} \tag{2}$$

$$b_i = e^{-S_i/R}e^{E_i \cdot 1000/RT} \tag{3}$$

The Langmuir parameter can be expressed using eq 3, where S_i is the site-specific molar entropy of adsorption in J/mol·K, E_i is the site-specific binding energy in kJ/mol, R is the gas constant in J/mol·K, and T is the temperature in K. The fitted parameters for CO and N_2 or H_2 adsorption can be found in Tables S2 and S3 (Supporting Information), respectively. Plots of the total adsorption isotherms with the corresponding single-, dual-, or triple-site Langmuir fits can be found in Figures S1–S6 (Supporting Information). Note that the CO adsorption isotherm data at 25, 35, and 45 °C were fit simultaneously for each material with a single set of parameters.

Isosteric Heat of Adsorption Calculations

Using the single-, dual-, and triple-site Langmuir fits, the isosteric heat of adsorption, $-Q_{st}$, was calculated for each compound as a function of the total amount of CO adsorbed using the Clausius–Clapeyron relation (eq 4).

$$-Q_{st} = RT^2 \left(\frac{\partial \ln P}{\partial T} \right)_n \tag{4}$$

where R is the ideal gas constant, P is the pressure, and T is the temperature.

Note that the isosteric heat of adsorption for a single-site Langmuir model is constant by definition. For dual- and triple-site Langmuir models, however, it is necessary to calculate the loading dependence of the isosteric heat of adsorption. As written, dual- and triple-site Langmuir equations specify the amount adsorbed as a function of pressure, while the pressure as a function of the amount adsorbed is needed to use the Clausius–Clapeyron relation. To calculate the isosteric heat of adsorption for evenly spaced loadings, each dual- and triple-site Langmuir equation was solved for the pressures that correspond to specific loadings at 25, 35, and 45 °C, and these calculated pressures were then used in eq 4 to determine the heat of adsorption as a function of the total amount of CO adsorbed. Note that the isosteric heat of adsorption is only reported over the CO loading range that was experimentally measured and mathematically fit for each compound.

Ideal Adsorbed Solution Theory Calculations

Since binary gas adsorption isotherms cannot be measured in a straightforward manner, it is often necessary to use an adsorption model, such as ideal adsorbed solution theory (IAST),(14) to predict mixed gas behavior from experimentally measured single-component isotherms. The accuracy of the IAST procedure has already been established for adsorption of a wide variety of different gases in zeolites and metal–organic frameworks.(12b, 15) Here, IAST is used to estimate the selectivity, S_{ads}, of all $M_2(dobdc)$ analogues for mixtures of CO and H_2 at 25 °C and a total pressure of 1 bar. Note that the selectivity factor, S, is defined according to eq 5, where n_i is the amount adsorbed of each component as determined from IAST and x_i is the mole fraction of each component in the gas phase at equilibrium.

$$S = \frac{n_{CO}/n_{H_2}}{X_{CO}/X_{H_2}} \tag{5}$$

It is important to note that calculated IAST selectivities are highly dependent on the adsorption model used to describe the single-component isotherm data. Specifically, isotherm fits at low pressures are most important for the strongest adsorbing component of a mixture (CO), while isotherms fits at high pressures are most important for the weakest adsorbing component (H_2). Here, the CO adsorption isotherms are very well described by single-, dual-, and triple-site Langmuir models for all $M_2(dobdc)$ frameworks, including in the steep low-pressure region of the isotherm (Figure S7, Supporting Information).

When fitting the H_2 isotherm data with Langmuir models, it is insufficient to consider just low-pressure adsorption, as was done for CO, even though the IAST calculations are performed at a total pressure of only 1 bar. This is because integrating the pure-component H_2 isotherms to calculate spreading pressure requires extrapolation to very high pressures. For instance, the IAST selectivity calculation for a 50:50 mixture of CO:H_2 in $Fe_2(dobdc)$ at 1 bar and 25 °C involves integrating the pure-component CO and H_2 isotherms up to 0.501 and 254 bar, respectively. As a result, the IAST selectivity is particularly sensitive to the H_2 saturation capacity, n_{sat}, of the Langmuir model. Since estimating the saturation capacity of H_2 from low-pressure isotherm data is difficult, high-pressure H_2 isotherms for $Ni_2(dobdc)$ and $Mg_2(dobdc)$ at 25 °C were used to estimate the high-pressure H_2

loadings when performing all isotherm fits. Note that the high-pressure H_2 data for Mg_2(dobdc) was previously reported,[16] while the high-pressure H_2 isotherm for Ni_2(dobdc) was measured in this work. While the IAST selectivities are sensitive to the fitted H_2 saturation capacity, this sensitivity does not significantly affect the overall magnitude of the calculated selectivity factor or of the trends between different M_2(dobdc) frameworks. This was confirmed by fitting the H_2 isotherm data for Ni_2(dobdc), Fe_2(dobdc), and Mg_2(dobdc) with a range of plausible H_2 saturation capacities and performing IAST calculations (Figure S8, Supporting Information).

High-Pressure Gas Adsorption

The high-pressure H_2 adsorption isotherm for Ni_2(dobdc) was measured on a HPVA-II-100 from Particulate Systems, a Micromeritics company. A detailed discussion of the accuracy of high-pressure measurements on this instrument was previously reported.[17] Here, 0.43 g of activated sample was loaded into a tared 2 mL stainless steel sample holder inside a glovebox under an N_2 atmosphere. Prior to connecting the sample holder to the VCR fittings of the complete high-pressure assembly inside the glovebox, the sample holder was weighed to determine the sample mass. The fully assembled sample holder was transferred to an ASAP 2020 low-pressure adsorption instrument, fitted with an isothermal jacket, and evacuated at the original activation temperature of the material for at least 1 h. Then, an N_2 adsorption isotherm was measured at 77 K. This data was used to verify that the high-pressure sample mass was correct and the sample was still of high quality by comparing the resulting Langmuir surface area to the expected. Note that a specially designed OCR adapter was used to connect the stainless steel high-pressure adsorption cell directly to the ASAP 2020 analysis port, allowing the measurement of accurate low-pressure isotherms on the exact same samples used for high-pressure measurements in the same sample holders. Prior to measuring Ni_2(dobdc), H_2 background measurements were performed at 25 °C on a sample holder containing nonporous glass beads that occupied a similar volume as a typical sample. A small positive background was observed, which may be due to errors in volume calibrations, temperature calibrations, and/or the equation of state used to perform the nonideality corrections. Regardless, the background H_2 adsorption was consistent across several measurements and was well described by a third order polynomial (Figure S9, Supporting Information). This polynomial was then used to perform a background subtraction on the raw high-pressure H_2 data for Ni_2(dobdc).

Infrared Spectroscopy

FTIR spectra were collected in transmission mode on a self-supported wafer of sample, in a controlled atmosphere using a custom-built infrared cell. The spectra were recorded at 2 cm^{-1} resolution on a Bruker IFS 66 FTIR spectrometer, equipped with a MCT detector. Adsorption and desorption of CO were followed at 77 K.

Mössbauer Spectroscopy

Mössbauer spectra of Fe_2(dobdc)·CO were measured at various temperatures between 20 and 275 K with a constant acceleration spectrometer, which utilized a rhodium matrix cobalt-57 source and was calibrated with α-iron foil. The absorber contained 55(1) mg/cm^2 of powder mixed with boron nitride. The absorber was prepared in an N_2-filled glovebox and placed in a Schlenk flask. The flask was removed from the glovebox, evacuated, and filled with CO. The sample was then cooled to 77 K with liquid nitrogen and inserted into a precooled cryostat under dry helium.

Magnetic Susceptibility

Magnetic data were collected using a Quantum Design MPMS-XL SQUID magnetometer. Measurements on Fe_2(dobdc) were obtained with finely ground microcrystalline powders restrained with a plug of glass wool within a sealed quartz tube. No effects of crystallite torqueing were

observed. Preparation of the CO-loaded sample was accomplished by attaching a sample of pure Fe_2(dobdc), loaded in a quartz tube, to a Micromeritics ASAP 2020 Surface Area and Porosity Analyzer. The pressure of the atmosphere of CO gas in the sample tube was then adjusted to 1 bar, the tube cooled in liquid N_2, and sealed with a hydrogen flame. Dc susceptibility measurements were collected in the temperature range of 2–300 K under a dc field of 1000 Oe. To avoid possible effects due to flash-freezing of the samples and sealed gas, the samples were cooled slowly from 300 to 2 K during the course of the measurement. Dc magnetic susceptibility data were corrected for diamagnetic contributions from the sample holder and glass wool, as well as for the core diamagnetism of each sample (estimated using Pascal's constants).[18]

Neutron Powder Diffraction

Neutron powder diffraction (NPD) experiments were carried out on activated M_2(dobdc) samples (M = Co, Fe, Mg, Mn, Ni, Zn) using the high-resolution neutron powder diffractometer, BT1, at the National Institute of Standards and Technology Center for Neutron Research (NCNR). The samples were placed in a He purged glovebox and 0.9702, 0.7286, 1.0010, 0.8576, 1.078, and 1.0761 g Co_2-, Fe_2-, Mg_2-, Mn_2-, Ni_2-, and Zn_2(dobdc), respectively, loaded into vanadium sample cans equipped with a gas loading valve, and sealed using an indium O-ring. NPD data were collected using a Ge(311) monochromator with an in-pile 60′ collimator corresponding to a wavelength of 2.078 Å. The samples were connected to a gas-manifold of known volume and exposed to a known dose of approximately 0.75 CO molecules per M^{2+} at 298 K (refined composition given in Tables S5–S12, Supporting Information). After equilibration times on the order of a hour, the sample cells were then placed in a dry ice bath to fully adsorb any residual CO, if any, as determined by a zero pressure reading on a pressure gauge and then allowed to equilibrate for another hour. The samples were sealed and allowed to further equilibrate at room temperature for several hours before loading onto a bottom-loading closed cycle refrigerator and slow cooling, to ensure full equilibration and complete adsorption, to 10 K for the data collection. In the case of Fe_2(dobdc), two subsequent gas doses, 1.5 and 2.0 CO per Fe^{2+}, were considered for comparability with our previous adsorption studies on this system, heating the sample in-line to 298 and 250 K, respectively, before dosing additional CO to ensure that the dose occurred above the temperature of the previous full equilibration and then slowly cooling to 10 K for data collection.[12b, 12c]

NPD data were analyzed using the Rietveld method as implemented in EXPGUI/GSAS.[19, 20] Starting models for the activated M_2(dobdc) frameworks were taken from our previous data on the bare materials and the atomic positions and isotropic atomic displacement parameters (ADPs) were left free to refine during the analysis process.[8e, 12b, 12c, 21] Fourier difference methods were employed to locate the adsorbed CO molecules. A dose of 0.75 CO per M^{2+} was chosen to provide clarity in the structure model for the active site in eliminating potential CO intermolecular interactions based on previous knowledge of adsorption in M_2(dobdc). In each instance, the CO atomic coordinates and isotropic ADPs were left free to refine, as was the occupancy of both the carbon and oxygen atoms. The carbon and oxygen atoms refined to identical occupancies within one standard deviation; however, these values were eventually constrained to be identical in each case for consistency. For all samples, the refined CO bond distance was equivalent to the accepted value for carbon monoxide within error; however, in the cases of Mn_2(dobdc) and Zn_2(dobdc), the value trended too long and was restrained to the ideal case, while in Co_2(dobdc), the distance trended too short and was also restrained to the ideal value. As per the structural discussion in the text, the result was a metal–carbonyl interaction via the carbon (M^{2+}–CO). In particular for the Mg_2(dobdc), but in several instances, the model was refined with the reverse orientation of the carbon monoxide (i.e., Mg–OC) and attempts to freely refine the CO in this orientation resulted in a very low occupancy for the carbon (with a negative isotropic ADP) and a very high occupancy for the oxygen atom (and very large isotropic ADP), as the model attempted to fit the available excess

scattering density almost entirely through the presence of the lone oxygen. This indicates the metal–carbonyl interaction is via the carbon with no possibility of a reverse conformation. The additional CO molecules in the refinement of the 1.5 and 2.0 CO per Fe^{2+} NPD data were refined with constrained C and O occupancies and bond distances, and free isotropic ADPs. The 1.5 CO per Fe^{2+} shows an additional adsorption site in the channels of the framework in a similar location as determined for the secondary physisorption oxygen site, but at a perpendicular geometry to O_2.[5] The third CO adsorption site, observed in the 2.0 CO dose, refines to a location in the very central portion of the channel furthest from the framework. This was modeled with very large isotropic ADPs indicative of a large positional disorder and potential condensation of CO in the channels at very high CO loadings.

Density Functional Theory Calculations

To study CO adsorption in M_2(dobdc) systems from first-principles, we used density functional theory within the generalized gradient approximation of Perdew, Burke, and Ernzerhof (PBE)[22] and a van der Waals dispersion-corrected functional.[23] The VASP program package[24] with a planewave basis set and projector augmented wave[25] pseudopotentials was used for all calculations. A Hubbard-like U parameter[26] was employed to better treat the localized d-states of the transition metal centers. We used an energy cutoff of 1000 eV for the planewave basis set and Brillouin zone sampling at the Γ-point, leading to binding energies that converged to within 1 kJ/mol.

To generate binding enthalpies, we first optimized periodic M_2(dobdc) crystals in a triclinic primitive unit cell of 54 atoms using a PBE+U approach, beginning from the experimental Zn_2(dobdc) structure and substituting in other divalent 3d transition metal cations (Mg, Mn, Fe, Co, and Ni) at all metal sites, until the residual forces were smaller than 0.01 eV/Å and the stress tensor components were smaller than 0.2 kbar. The computed lattice parameters are all within 2% of the experimental results. For open-shell cations, we employ Hubbard-like U corrections. Values of U used were 4.0, 4.0, 3.3, and 6.4 eV for Mn, Fe, Co, and Ni, respectively; these values were taken from ref 27, where they were determined for each metal center to reproduce the experimental oxidation energy of the metal-monoxide to M_2O_3. For all M_2(dobdc) compounds, we found a high-spin ground state, and then assumed ferromagnetic ordering along the metal-oxide chain direction and antiferromagnetic ordering between the chains, as observed experimentally for the ground state magnetic ordering within Fe_2(dobdc).[28]

To predict adsorption geometries, molecules were relaxed inside rigid periodic M_2(dobdc) frameworks using vdW–DF2+U (ref 23) at a loading of one molecule per six metal sites. vdW–DF2 was shown in previous work to provide excellent binding energetics for CO_2 adsorption in M_2(dobdc) systems.[29] vdW–DF2+U was also used in single-point calculations to compute the energies of the bare M_2(dobdc) compounds for use in calculating binding enthalpies.

Binding enthalpies at 308 K were calculated by including quantum zero-point energies (ZPEs) and finite-temperature thermal energies (TEs) at the level of a harmonic approximation. The enthalpy of adsorption of a molecule in a MOF is calculated as

$$-\Delta H = H(\text{CO} + \text{MOF}) - H(\text{CO}) - H(\text{MOF})$$

where H(MOF), H(CO), and H(CO + MOF) are the enthalpies of the bare MOF without CO, the enthalpy of CO in the gas phase, and the enthalpy of the MOF with CO adsorbed, respectively.

ETS-NOCV Analysis

Cluster models were cropped from the experimental crystal structures, as shown in Figure S23 (Supporting Information). This model was designed[30] to retain the local structure of framework

about the central metal ion while remaining small enough for the electronic structure calculations. For M = Mn, Fe, Co, Ni, the two exterior metal sites were substituted by closed shell Zn^{II} centers while the central metal that binds the CO remained in its high-spin (ground) state. Hydrogen atoms were used to cap the truncated cluster model.

Constrained geometry optimizations were performed where the experimental framework and CO were held fixed while the capping H atoms from the cluster truncation were relaxed. The PBE functional[31] was used in the TURBOMOLE V6.4 2012[32] software package. Resolution of the identity (RI)[33, 34] and associated auxiliary basis functions[35-37] were employed. The def2[38] basis sets were used. For metal, oxygen, and the binding CO the def2-TZVP basis set was used, while for all C and H the def2-SVP basis set was used.

Bond Analysis

The extended transition state (ETS) method for energy decomposition, combined with the natural orbitals for chemical valence (NOCV) theory (ETS-NOCV)[39] was used to decompose the metal-CO bond into different components (e.g., σ, π) and evaluate the magnitudes of their contributions to the total bond energy. This analysis was performed with the Amsterdam Density Functional (ADF) version 2013 software package.[40-42] The M06-L functional[43] was used with the DZP basis set and an increased integration grid of 8. The zeroth order regular approximation (ZORA) was used to treat relativistic effects.

Results and Discussion

Infrared Spectroscopy

As an initial probe of the interaction of CO with the square pyramidal M^{2+} cations lining the ~12-Å wide channels in M_2(dobdc), we turned to in situ infrared spectroscopy (Figure 1).[44] For all six frameworks, a single adsorption band is observed at low coverage between 2160 and 2178 cm^{-1},[45] which is blue-shifted with respect to the stretching mode of free CO (2143 cm^{-1})[45] (see the Supporting Information for further details on the infrared spectra). These values are consistent with those previously reported for M^{2+} ions in weak ligand field environments.[3] Most metal-CO interactions feature a synergistic interaction between σ charge donation and π back-donation.[46, 47] For classical transition metal carbonyl complexes, the average υ(CO) is red-shifted, because the M → CO π back-donation is the dominant effect, significantly weakening the C–O bond compared to that of free CO. When back-donation is absent or diminished, υ(CO) is blue-shifted in a phenomenon that is termed nonclassical CO adsorption. Of the more than 20 000 reported M–CO stretching frequencies, only approximately 250–300 can be considered nonclassical.[3b]
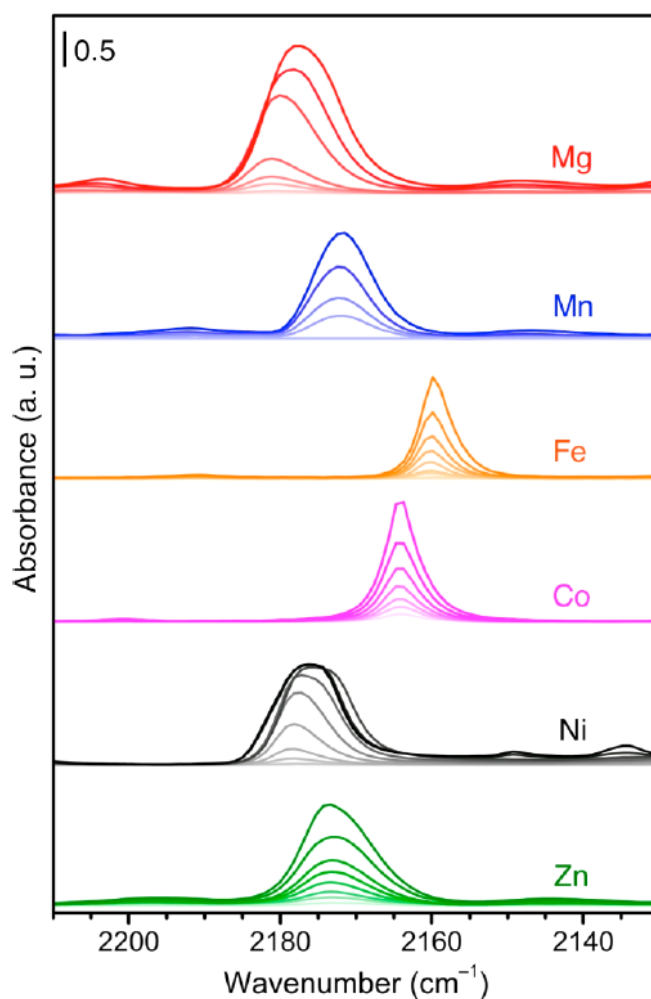
Figure 1. Background subtracted FTIR spectra of M$_2$(dobdc) collected at 77 K in the presence of CO. Light to dark lines represent increasing CO coverages on samples preactivated at 453 K. The C–O stretching frequencies for all six metals are blue-shifted with respect to free CO (2143 cm^{-1}).

Of the six materials investigated, carbonyl coordination is most simply described within Mg$_2$(dobdc) and Zn$_2$(dobdc). The Mg^{2+} ions in the former lack d electrons and are thus unable to back-donate into the empty CO π* orbitals. Additionally, the empty Mg 3d levels are high in energy and do not provide a good match for σ donation from the lone pair electrons of CO. The Mg^{2+}–CO interaction is thus primarily electrostatic in nature, an effected that is expected to increase the C–O stretching frequency as the CO bonding orbitals become less polarized toward the more electronegative oxygen and thus more covalent.(48) As a result, Mg$_2$(dobdc) displays the highest-energy infrared stretch of 2178 cm^{-1}, consistent with those reported for CO adsorption in Mg^{2+}-exchanged zeolites.(49) On the other hand, the Zn^{2+} ions in Zn$_2$(dobdc) have a fully occupied set of 3d orbitals that are therefore not available to accept σ donation from CO, resulting in a similarly high infrared stretch of 2173 cm^{-1}. In both cases, the metal–carbonyl interaction is primarily a result of ion-induced dipole interactions. Similar behavior is observed in the case of Mn$_2$(dobdc), in which the υ(CO) of 2172 cm^{-1} is red-shifted with respect to Mg$_2$(dobdc), as a result of diminished polarization by the larger-radius, softer Mn^{2+} ions and presumably only a very small, nearly negligible π backbonding contribution. The metal ions in both Fe$_2$(dobdc) and Co$_2$(dobdc) are smaller and more polarizing than Mn^{2+}; however, the C–O stretching frequencies displayed by these materials (2160 cm^{-1} for Fe^{2+} and 2164 cm^{-1} for Co^{2+}) are the lowest reported here, suggesting slightly more pronounced π interactions. The compound Ni$_2$(dobdc) displays the highest CO

10

stretching frequency among the transition metal cations (2178 cm^{-1}), since Ni^{2+} is the smallest and most polarizing ion. Given the small, charge-dense nature of Ni^{2+}, its lower energy π-type 3d orbitals are less well-suited for back-donation into CO than either Fe^{2+} or Co^{2+}.
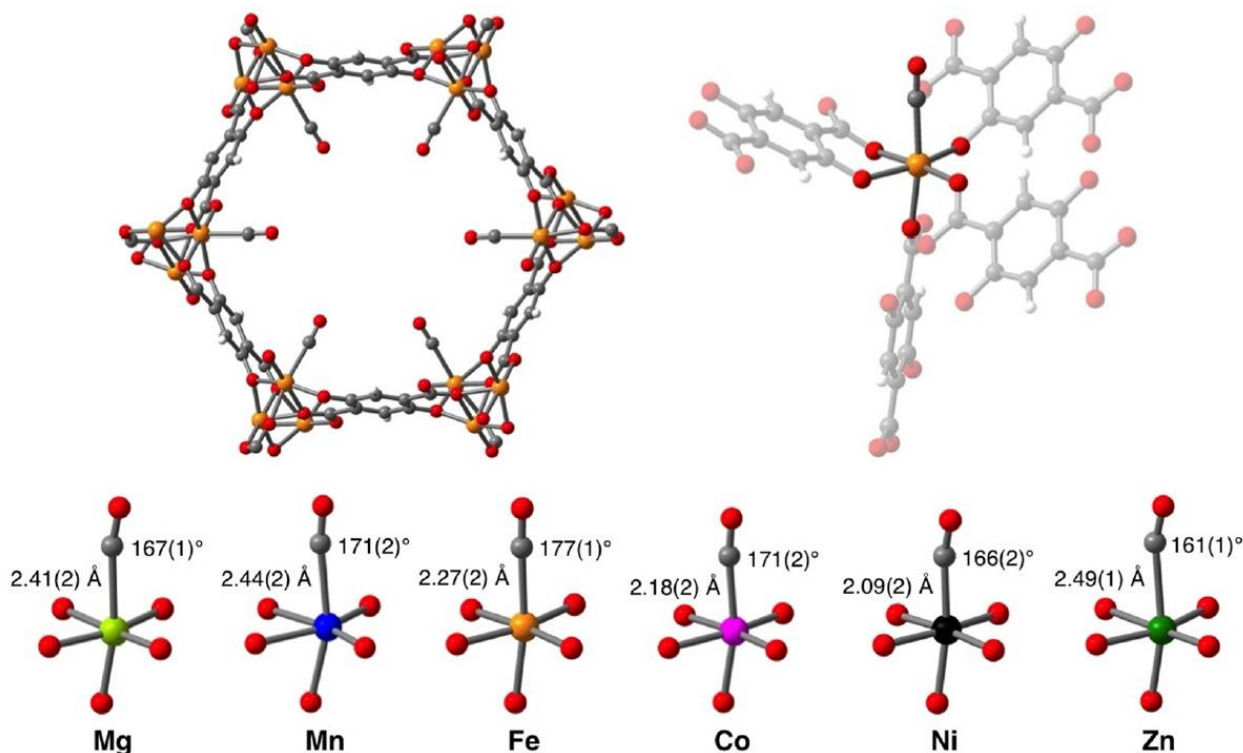
Figure 2. Structures from powder neutron diffraction. (Upper left) A view down a channel (along the *c* axis) in the structure of Fe$_2$(dobdc)·1.5CO, as determined by Rietveld analysis of powder neutron diffraction data. At this loading, the occupancy of the metal-bound CO molecules are all close to the expected value of 75%. (Upper right) Coordination environment for a single Fe^{2+} site in Fe$_2$(dobdc)·1.5CO. (Lower) First coordination sphere for the M^{2+} ions in M$_2$(dobdc)·1.5CO, with M–CO distances and M–C–O angles indicated.

Structural Characterization

Given our prior success in elucidating crystal structures of a number of adsorbent molecules in M$_2$(dobdc),(8g, 12b, 12c) we turned to neutron powder diffraction experiments to further characterize the carbonyl adducts M$_2$(dobdc)·1.5CO (Figure 2). Consistent with the large range in CO infrared stretching frequencies, we see a range of M–C–O angles, from 161.2(7)° for Zn to 176.9(6)° for Fe, in excellent agreement with previous calculations on the Mg, Ni, and Zn analogues,(50) and with a good correlation observed between υ(CO) and the M–C–O angle (Figure 3). In the cases of the Fe and Co homologues, where a greater degree of π backbonding is observed via infrared spectroscopy, more linear carbonyl adducts are formed, while in the cases where electrostatic effects play a major role, bent structures are observed. Additionally, the structures display a large range in M–C bond distances, ranging from 2.09(2) Å for Ni to 2.49(1) Å for Zn, with an excellent correlation between adsorption enthalpy and M–C distance (Figure 3). The Mn, Fe, Co, and Ni frameworks bind CO with M–CO distances of 2.44(2), 2.27(2), 2.18(2) and 2.09(2) Å, respectively, a trend that is consistent with the Irving–Williams stability order. The value for Ni is in good agreement with what was previously found from EXAFS data and ab initio molecular modeling.(51)
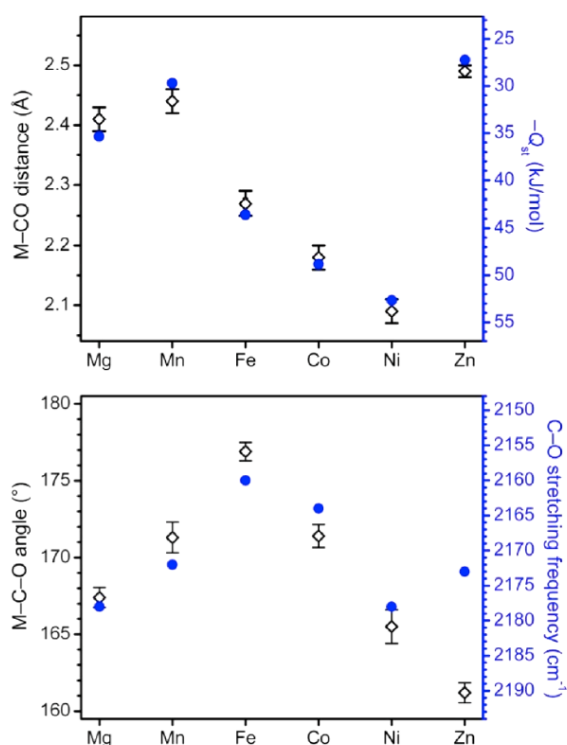
Figure 3. (Upper) Variations of M–C–O angle (open black diamonds) and C–O stretching frequency (blue circles) with metal center in M_2(dobdc), indicating the correlation between greater backbonding and a more linear metal–carbonyl adduct. (Lower) Variations of M–CO distance (open black diamonds) and isosteric heat of CO adsorption (Q_{st}, blue circles) with metal center in M_2(dobdc). Error bars indicate the estimated standard deviations from the crystal structure refinements.

Overall, these distances are much longer than those typically found for divalent first-row transition metal carbonyl complexes, which rarely exceed 2.0 Å.[(3)] Divalent manganese carbonyl complexes, often generated by the chemical[(52)] or electrochemical[(53)] one-electron oxidation of analogous manganese(I) complexes, are low-spin and feature Mn–C distances below 1.9 Å. A number of iron(II)–carbonyl species obtained by the binding of CO to coordinatively unsaturated iron cations of various overall coordination numbers have been isolated.[(4)] In all but three cases, the iron cations in these molecules are diamagnetic upon CO coordination and display Fe–C distances of 1.75 to 1.90 Å. Both nickel(II)– and cobalt(II)–carbonyl are similarly rare and feature low-spin metal cations and short M–C distances.[(54)] The unusually long M–C distances observed here are a result of the weak field oxo-donors of dobdc^{4-} and the framework lattice enforcing an unprecedented high-spin configuration for each of these metals in the presence of CO. Furthermore, Mg_2(dobdc)·1.5CO and Zn_2(dobdc)·1.5CO, with M–CO distances of 2.41(2) and 2.49(1) Å, respectively, represent the first crystallographically characterized magnesium and zinc carbonyl complexes, regardless of oxidation state.[(49, 55)]

Spin-State Characterization

Magnetic susceptibility data were collected to confirm the high-spin character of the iron(II) centers in the CO-adsorbed phase Fe_2(dobdc)·2CO. At 300 K, the value of $\chi_M T$ for Fe_2(dobdc) is 6.40 cm^3 K/mol, slightly higher than that expected (6.00 cm^3 K/mol) for two high-spin ($S = 2$) iron(II) centers with $g = 2.00$.[(12b)] As the temperature is lowered, $\chi_M T$ gradually increases, reaching 7.88 cm^3 K/mol at 28 K, before dropping to 1.01 cm^3 K/mol at 2 K. In contrast, when dosed with carbon monoxide gas, Fe_2(dobdc)·2CO displays a monotonic decrease in $\chi_M T$ with lowering temperature, falling from 6.49 cm^3 K/mol at 300 K (consistent with high-spin iron(II)) to 0.39 cm^3 K/mol at 2 K.

The arrangement of metal ions in $Fe_2(dobdc)$ suggests two dominant magnetic interactions: magnetic coupling between ions along each chain and coupling between ions belonging to different chains. The Fisher model[56] was employed with a molecular field approximation[57] to fit the data and extract the relative strengths of these interactions for $Fe_2(dobdc)\cdot2CO$, as has been done in previous work.[12][e] The specific Hamiltonian used is represented as eq 6.

$$\hat{H} = -2J \sum_i \mathbf{S}_{Fe(i)}\mathbf{S}_{Fe(i+1)} - M\mathbf{B} \sum_i \mathbf{S}_{Fe(i)} - zJ'\langle S_{Fe}\rangle\mathbf{S}_{Fe} \qquad (6)$$

In eq 6, J is the intrachain Fe–Fe superexchange coupling constant, and $\mathbf{S}_{Fe(i)}$ and $\mathbf{S}_{Fe(i+1)}$ are the spin operators for the iron ions of the chain. $M\mathbf{S}_{Fe(i)}$ corresponds to the magnetic moment of the Fe(i) spin, $\mathbf{B}$ is the applied field, z the number of interacting nearest-neighbors, J' the interchain coupling constant, and $\langle S_{Fe}\rangle$ the mean value of the S_z component of the S_{Fe} operator. In this model, a positive sign for J and J' indicates a ferromagnetic interaction while a negative sign indicates an antiferromagnetic interaction. The best fits for $Fe_2(dobdc)\cdot2CO$ yielded $J = -1.6(2)$ cm^{-1} and $J' = -1.12(2)$ cm^{-1}, in contrast to $J = -4.12(6)$ cm^{-1} and $J' = -1.12(1)$ cm^{-1} for the bare framework (Figure S21, Supporting Information). Note that zero-field splitting was not accounted for with this analysis but could be substantial.[58] Previous work on the magnetic susceptibility of $Fe_2(dobdc)$ in the presence of gases revealed a strong correlation between gas-binding strength and intrachain magnetic coupling.[12b] Weakly binding gases weakened the magnitude of J but retained the sign. In contrast, strongly binding gases served to change the electron density around the iron(II) ions enough to invert the intrachain coupling from ferro- to antiferromagnetic in nature. As seen for $Fe_2(dobdc)\cdot2CO$, $\chi_M T$ plots of the framework under strongly binding gases are thus devoid of any maximum at low temperatures.

Mössbauer spectra further confirm the assignments of high-spin iron(II) (Figure S22, Supporting Information). In the absence of CO, the spectra of $Fe_2(dobdc)$ feature a simple quadrupole doublet, which at 40 K exhibits an isomer shift of 1.094(3) mm/s and a quadrupole splitting of 2.02(1) mm/s. In the presence of CO, these values shift slightly to 1.198(5) and 2.60(1) mm/s, respectively, consistent with high-spin iron(II) in an octahedral coordination environment. The result for $Fe_2(dobdc)\cdot2CO$ is without precedent. Of the nearly 9,000 iron–carbonyl structures reported in the Cambridge Crystal Structure Database, only three are paramagnetic, all featuring intermediate-spin ($S = 1$) iron(II) centers in a trigonal bipyramidal coordination environment, for which an $S = 0$ spin state is generally not possible.[59] Thus, $Fe_2(dobdc)\cdot2CO$ represents the first example of a paramagnetic octahedral iron carbonyl compound and, to our knowledge, the first reported $S = 2$ iron carbonyl.
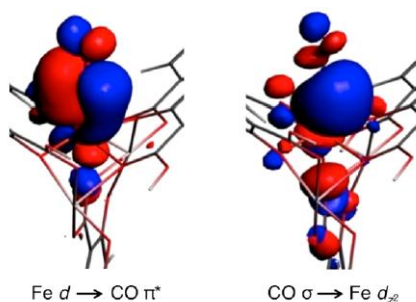
Electronic Structure Calculations

Density functional theory calculations (vdW–DF2+U) were employed to explore CO binding from first principles. To account for distortions in the framework structure upon binding, CO-metal distances were fixed as predicted by the vdW–DF2+U calculation and a subsequent relaxation of the MOF+CO system was performed at the PBE+U level. A final relaxation of CO in the rigid but distorted MOF was then performed at the vdW–DF2+U level. This procedure leads to good agreement for both local adsorption geometries (which are well described with vdW–DF2+U) *and* lattice parameters (which are better described by PBE+U). As shown in Figure 4, we see excellent agreement between predicted and experimental values for a number of metrics. Specifically, DFT predicts blue-shifted CO stretching frequencies upon coordination to all six frameworks, with $Fe_2(dobdc)$ displaying the least blue-shifted value. Accordingly, DFT also predicts a wide range of

M–C–O angles. Although the calculated M–CO distances are slightly overestimated, from 0.12 Å for Mg to 0.27 Å for Ni, a known tendency of the vdW–DF2 functional, the trend in binding distance is captured quite accurately. Importantly, DFT predicts the Mn, Fe, Co, and Ni frameworks to have a high-spin ground state, which is maintained upon CO coordination. The accuracy of these DFT calculations is quite important as it can be extended to metal–organic frameworks for which synthetic conditions have yet to be realized.(11)
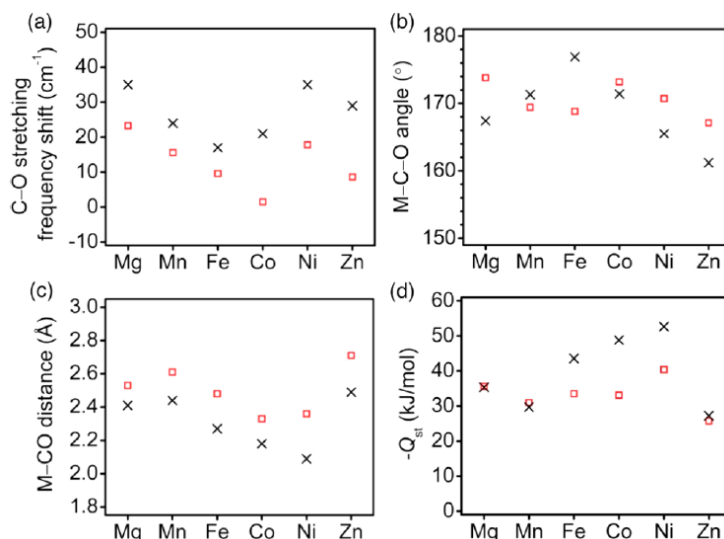
Figure 4. DFT calculated C–O stretching frequency shift relative to free isolated CO (upper left), M–C–O angle (upper right), M–CO distance (lower left), and binding enthalpy (lower right) in M$_2$(dobdc) in comparison to experimental values (black cross marks).

Fe $d \rightarrow$ CO π^* CO $\sigma \rightarrow$ Fe d_{z^2}

Figure 5. Contours of orbitals involved in CO binding in Fe$_2$(dobdc).

We also utilized electronic structure calculations to investigate the relative strength of the metal–CO π^* back-donation by using the extended transition state (ETS) method, in combination with natural orbitals for chemical valence (NOCV) theory. The resulting contours are plotted in Figure S23 (Supporting Information). The largest eigenvalues that have π^* CO character are shown, along with the magnitude of their ΔE_{orb} contributions. The purpose of this decomposition is to gain a qualitative interpretation of the nature of this bond for M = Mn, Fe, Co, and Ni between two predefined fragments. In this case, fragment 1 (F1) was chosen to be the model cluster of the M$_2$(dobdc), and fragment 2 (F2) was chosen to be CO. From performing calculations on the two isolated fragments (in their complexed geometry) and then performing a calculation on the complex, a deformation density is calculated. This may then be partitioned into the NOCVs, which have just a few significant contributors to the bond. The sums of these ΔE_{orb} terms involving CO π^* orbitals are reported in Table S13 (Supporting Information). In agreement with the interpretation of the infrared spectra, iron displays the strongest π back-bonding contribution, with Fe > Co > Ni $\gg$ Mn. A comparison of the relative energy contributions for σ- and π-type interactions reveals that

14

back-bonding is the more important orbital interaction. As examples, the canonical molecular orbital with the largest contribution to CO binding in $Fe_2(dobdc)$ is plotted in Figure 5. Bond analysis indicates that Fe → CO π back-donation accounts for approximately 70% of the orbital interaction energy. The same trend is found for Mn, Co, and Ni, and is expected as d_{z2} is singly occupied when these ions are in a high-spin octahedral coordination environment and thus poorly suited for CO → M σ donation.

Gas Adsorption

To investigate the CO uptake within these frameworks under various conditions, pure component adsorption isotherms were measured at 298, 308, and 318 K, and isosteric heats of adsorption were calculated for each metal (Figure 6, Table 1). At 298 K, the CO adsorption isotherms for the Fe, Co and Ni frameworks approach the value expected for one CO molecule per open metal site. The loading capacities for these materials, which climb as high as 6.0 mmol/g and 156.8 cm^3/cm^3 for $Fe_2(dobdc)$ at 298 K and 1.2 bar, are much greater than typically observed in metal–organic frameworks, a result of the high gravimetric density of open metal sites in the structures. Importantly, in all cases, the bound CO could be completely desorbed upon application of dynamic vacuum and/or heat, and subsequent CO adsorption isotherms showed no loss of uptake capacity. The isosteric heats of adsorption calculated from the data vary widely with metal, from −52.7 to −27.2 kJ/mol, with the CO binding strength following the order Ni > Co > Fe > Mg > Mn > Zn (Figure 6). The trend is in distinct contrast to that observed for CO_2 adsorption in these materials, an interaction that is predominately electrostatic in nature, where the Mg framework displays the highest binding enthalpy.(60) This suggests, as discussed above, that the coordination of carbon monoxide is not purely a result of electrostatics, but indeed involves some σ and π orbital interactions.
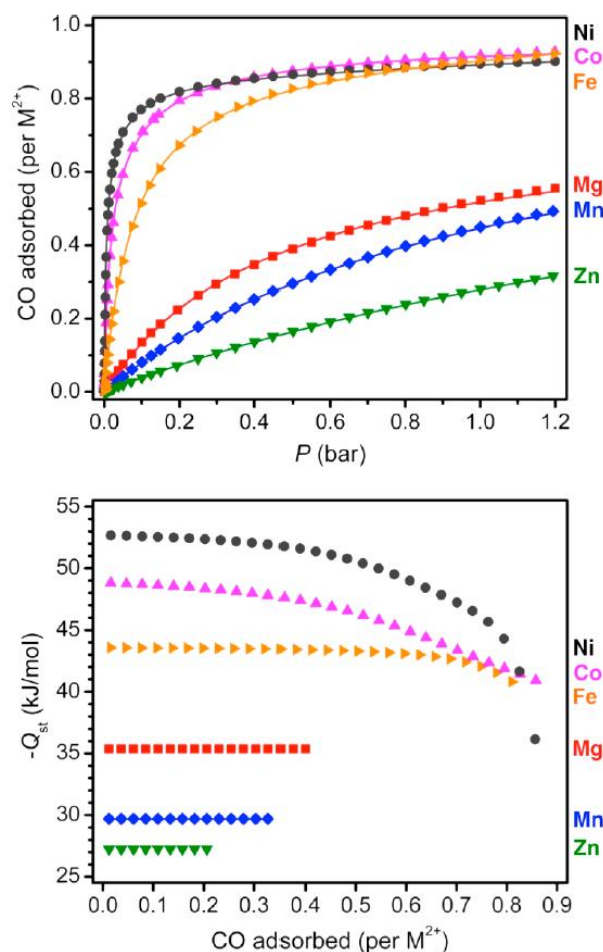
Isosteric heats of CO adsorption computed within a harmonic approximation agree with the experimental trend,(50) predicting isosteric heats of adsorption from −25.7 kJ/mol for Zn to −40.4 kJ/mol for Ni at 308 K. The comparison of calculated values to experimentally determined values of isosteric heats of adsorption is shown in Figure 4d. We note that the largest discrepancies arise for the metal centers that give rise to the strongest orbital interactions: Fe, Co, and Ni.

Table 1. Isosteric Heat of CO Adsorption, M−C Distance, M−C−O Angle, CO Capacity, CO/H$_2$ and CO/N$_2$ IAST Selectivities for M$_2$(dobdc)

	-Q$_{st}$ (kJ/mol)	M−C dist. (Å)	M−C−O angle (deg)	1.2 bar CO capacity^a (mmol/g)	CO/H$_2$ IAST selectivity		CO/N$_2$ IAST selectivity	
					CO:H$_2$ 0.333	CO:H$_2$ 1.0	CO:N$_2$ 0.333	CO:N$_2$ 1.0
Mg	35.4	2.41(2)	167(1)	4.58	188 (98.4)^b	170 (99.4)	11.3 (79.0)	10.3 (91.2)
Mn	29.7	2.44(2)	171(1)	3.24	91 (96.8)	86 (98.9)	10.7 (78.2)	10.3 (91.1)
Fe	43.6	2.27(2)	177(1)	6.04	634 (99.5)	507 (99.8)	80 (96.4)	68 (98.5)
Co	48.8	2.18(2)	171(2)	5.95	1420 (99.8)	1040 (99.9)	206 (98.6)	163 (99.4)
Ni	52.7	2.09(2)	166(2)	5.79	2448 (99.9)	1705 (99.9)	289 (99.0)	216 (99.5)
Zn	27.2	2.49(2)	161(1)	1.95	49 (94.2)	47 (97.9)	7.6 (71.7)	7.5 (88.2)

^{a}Total adsorption at 298 K. ^{b}Values in parentheses represent the purity of CO gas achievable for the given selectivity.

Figure 6. (Upper) Carbon monoxide isotherms measured at 298 K. For the Fe, Co, and Ni analogues, CO uptake approaches one molecule per metal cation site at 1.2 bar. (Lower) Isosteric heats of CO adsorption calculated from isotherms measured at 298, 308, and 318 K.

The extraordinary ability of these materials to bind CO reversibly and at high capacity suggests their application in removing CO from gas mixtures, such as CO/N_2[61, 62] and CO/CH_4,[63] and, in particular, for the purification of CO from syngas. In order to determine the CO/H_2 selectivities, we employed ideal adsorbed solution theory (IAST),[64] the accuracy of which has already been established for adsorption of a wide variety of different gases in zeolites and metal–organic frameworks (see the Supporting Information for details on the IAST calculations).[65] To reflect the varying H_2:CO ratios found in syngas, IAST selectivities were calculated over a range of compositions (Figure 7), and were found to vary widely, from a minimum of 45 in the case of Zn_2(dobdc) to over 5200 for Ni_2(dobdc) at low CO concentrations. Significantly, these selectivities are all much higher than those observed for metal–organic frameworks lacking coordinatively unsaturated metal cations, such as the value of 2.7 determined for MOF-5.[66]

The IAST selectivities are indicative of the purity at which CO could be produced in a separation, with, for example, the values of 47 and 1705 for an equimolar CO/H_2 mixture at 1 bar and 298 K enabling Zn_2(dobdc) and Ni_2(dobdc) to produce CO with purities of 97.9% and 99.9%, respectively. Thus, the importance of having materials exhibiting a range of different CO binding energies becomes clear: one can select the M_2(dobdc) compound that will provide just the minimum level of CO purity required, thereby minimizing the regeneration energy associated with CO desorption. Finally, we note that the high CO/N_2 selectivities of these materials (Figure 7) bodes particularly well for their use in the separation of CO from syngas contaminated with N_2.
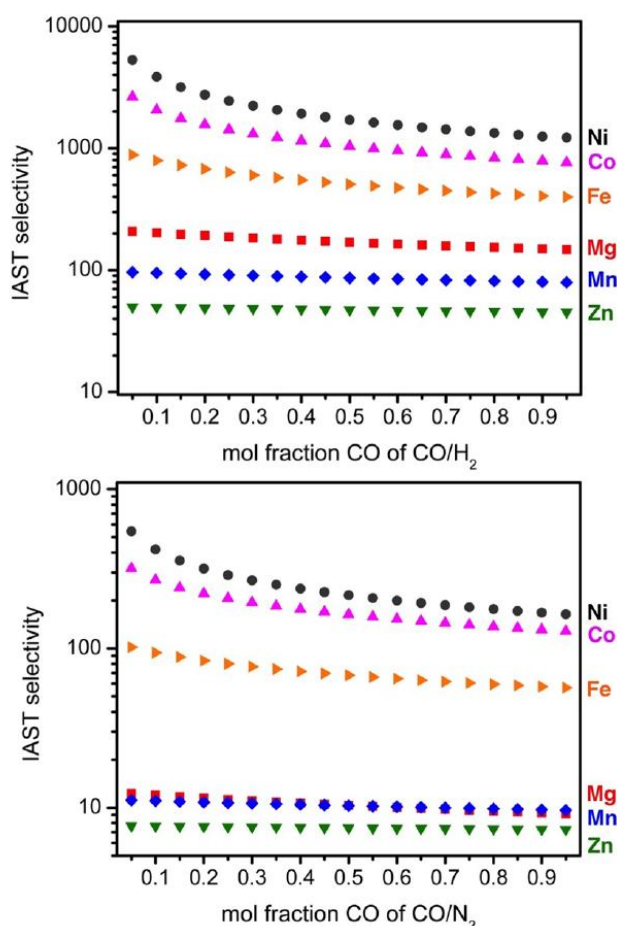
Figure 7. Ideal adsorbed solution theory (IAST) selectivities for mixtures of CO/H_2 (upper) and CO/N_2 (lower) of varying compositions at 298 K and 1 bar.

Conclusions

Metal–organic frameworks of the $M_2(dobdc)$ structure type provide an excellent platform for the investigation of new coordination chemistry via gaseous substrate binding at coordinatively unsaturated metal sites. Significantly, the weak ligand field presented by the oxo and carboxylate donor ligands enforces a high-spin electron configuration for the divalent metal cations, even in the presence of the prototypical strong field ligand CO. The rigidity of the evacuated materials, together with their highly crystalline nature, has thus enabled the generation and crystallographic characterization of the first high-spin manganese(II), iron(II), cobalt(II), and nickel(II) carbonyl species, as well as the first magnesium and zinc carbonyls. The fully reversible CO binding at high capacity and moderate adsorption enthalpies further make these materials outstanding candidates for applications in the efficient separation of CO from more weakly adsorbing gases, such as H_2 and N_2.

Supporting Information

Additional gas adsorption, structural, and spectroscopic data as well as further computational details. This material is available free of charge via the Internet at http://pubs.acs.org.

The authors declare no competing financial interest.

Acknowledgment

References

(1) (a) Welch, A. J. E. Rep. Prog. Chem. 1941, 38, 71−83. (b) Anderson, J. S. Q. Rev. Chem. 1947, 1, 331−357.

(2) (a) Schützenberger, C. R. Bull. Soc. Chim. Paris 1868, 10, 188−192. (b) Ellis, J. E.; Beck, W. Angew. Chem., Int. Ed. Engl. 1995, 34, 2489−2491. (c) Timney, J. A. Organomet. Chem. 1999, 27, 132−150.

(3) (a) Aubke, F.; Wang, C. Coord. Chem. Rev. 1994, 137, 483−524. (b) Lupinetti, A. J.; Strauss, S. H.; Frenking, G. Prog. Inorg. Chem. 2001, 49, 1−112.

(4) Benito-Caragorri, D.; Lagoja, I.; Veiros, L. F.; Kirchner, K. A. Dalton Trans. 2011, 40, 4778−4792.

(5) Kerry, F. G. Industrial Gas Handbook: Gas Separation and Purification; CRC: Boca Raton, FL, 2007.

(6) McCandless, F. P. Ind. Eng. Chem. Process Des. Dev. 1972, 11, 470−478.

(7) Miyajima, H.; Kodama, A.; Goto, M.; Hirose, T. Adsorption 2005, 11, 625−630.

(8) (a) Rosi, N. L.; Kim, J.; Eddaoudi, M.; Chen, B.; O'Keeffe, M.; Yaghi, O. M. J. Am. Chem. Soc. 2005, 127, 1504−1518. (b) Dietzel, P. D. C.; Morita, Y.; Blom, R.; Fjellvåg, H. Angew. Chem., Int. Ed. 2005, 44, 6354−6358. (c) Dietzel, P. D. C.; Panella, B.; Hirscher, M.; Blom, R.; Fjellvåg, H. Chem. Commun. 2006, 959−961. (d) Dietzel, P. D. C.; Blom, R.; Fjellvåg, H. Eur. J. Inorg. Chem. 2008, 3624−3632. (e) Zhou, W.; Wu, H.; Yildirim, T. J. Am. Chem. Soc. 2008, 130, 15268−15269. (f) Caskey, S. R.; Wong-Foy, A. G.; Matzger, A. J. J. Am. Chem. Soc. 2008, 130, 10870−10871. (g) Bloch, E. D.; Murray, L. J.; Queen, W. L.; Chavan, S.; Maximoff, S. N.; Bigi, J. P.; Krishna, R.; Peterson, V. K.; Grandjean, F.; Long, G. J.; Smit, B.; Bordiga, S.; Brown, C. M.; Long, J. R. J. Am. Chem. Soc. 2011, 133, 14814−14822.

(9) (a) Mason, J. A.; Sumida, K.; Herm, Z. R.; Krishna, R.; Long, J. R. Energy Environ. Sci. 2011, 4, 3030−3040. (b) Férey, G.; Serre, C.; Devic, T.; Maurin, G.; Jobic, H.; Llewellyn, P. L.; De Weireld, G.; Vimont, A.; Daturi, M.; Chang, J.-S. Chem. Soc. Rev. 2011, 40, 550−562. (c) Li, J.-R.; Sculley, J.; Zhou, H.-C. Chem. Rev. 2012, 112, 869−932.

(10) Herm, Z. R.; Swisher, J. A.; Smit, B.; Krishna, R.; Long, J. R. J. Am. Chem. Soc. 2011, 133, 5664−5667.

(11) Lee, K.; Isley, W. C.; Dzubak, A. L.; Verma, P.; Stoneburner, S. J.; Lin, L.-C.; Howe, J. D.; Bloch, E. D.; Reed, D. A.; Hudson, M. R.; Brown, C. M.; Long, J. R.; Neaton, J. B.; Smit, B.; Cramer, C. J.; Truhlar, D. G.; Gagliardi, L. J. Am. Chem. Soc. 2013, 136, 698−704.

(12) (a) Zhang, Z.; Xiang, S.; Chen, B. CrystEngComm 2011, 13, 5983−5992. (b) Bloch, E. D.; Queen, W. L.; Krishna, R.; Zadrozny, J. M.; Brown, C. M.; Long, J. R. Science 2012, 335, 1606−1610. (c) Bae, Y.-S.; Lee, C. Y.; Kim, K. C.; Farha, O. K.; Nickias, P.; Hupp, J. T.; Nguyen, S. T.; Snurr, R. Q. Angew. Chem., Int. Ed. 2012, 51, 1857− 1860. (d) Geier, S. J.; Mason, J. A.; Bloch, E. D.; Queen, W. L.; Hudson, M. R.; Brown, C. M.; Long, J. R. Chem. Sci. 2013, 4, 2054−2061.

(13) (a) Lemmon, E. W.; Span, R. J. Chem. Eng. Data 2006, 51, 785−850. (b) Lemmon, E. W.; Huber, M. L.; McLinden, M. O. NIST Standard Reference Database 23: Reference Fluid Thermodynamic and Transport Properties-REFPROP, Version 8.0; National Institute of Standards and Technology, Standard Reference Data Program: Gaithersburg, MD, 2007. (c) Leachman, J. W.; Jacobsen, R. T.; Lemmon, E. W. J. Phys. Chem. Ref. Data 2009, 38, 721−748.

(14) Myers, A. L.; Prausnitz, J. M. AIChE J. 1965, 11, 121−127.

(15) (a) Krishna, R.; Calero, S.; Smit, B. Chem. Eng. J. 2002, 88, 81−94. (b) Krishna, R.; van Baten, J. M. Chem. Eng. J. 2007, 133, 121. (c) Krishna, R.; van Baten, J. M. Phys. Chem. Chem. Phys. 2011, 13, 10593−10616.

(16) Sumida, K.; Brown, C. M.; Herm, Z. R.; Chavan, S.; Bordiga, S.; Long, J. R. Chem. Commun. 2011, 47, 1157−1159.

(17) Mason, J.; Veenstra, M.; Long, J. R. Chem. Sci. 2014, 5, 32−51.

(18) Bain, G. A.; Berry, J. F. J. Chem. Educ. 2008, 85, 532.

(19) Toby, B. H. J. Appl. Crystallogr. 2001, 34, 210−213.

(20) Larson, A. C.; Von Dreel, R. B. Los Alamos Natl. Lab., [Rep.] LA (U. S.) 1994, 86−748.

(21) Queen, W. L.; Bloch, E. D.; Brown, C. M.; Hudson, M. R.; Mason, J. A.; Murray, L. J.; R.-Cuesta, A. J.; Peterson, V. K.; Long, J. R. Dalton Trans. 2012, 41, 4180−4187.

(22) Perdew, J.; Burke, K.; Ernzerhof, M. Phys. Rev. Lett. 1996, 77, 3865.

(23) Lee, K.; Murray, É. D.; Kong, L.; Lundqvist, B. I.; Langreth, D. C. Phys. Rev. B: Condens. Matter Mater. Phys. 2010, 82, 081101.

(24) Kresse, G.; Joubert, D. Phys. Rev. B: Condens. Matter Mater. Phys. 1999, 59, 1758−1775.

(25) Blöchl, P. E. Phys. Rev. B: Condens. Matter Mater. Phys. 1994, 50, 17953−17979.

(26) (a) Anisimov, V. I.; Zaanen, J.; Andersen, O. K. Phys. Rev. B: Condens. Matter Mater. Phys. 1991, 44, 943. (b) Dudarev, S. L.; Botton, G. A.; Savrasov, S. Y.; Humphreys, C. J.; Sutton, A. P. Phys. Rev. B: Condens. Matter Mater. Phys. 1998, 57, 1505.

(27) Wang, L.; Maxisch, T.; Ceder, G. Phys. Rev. B: Condens. Matter Mater. Phys. 2006, 73, 195107−195112.

(28) Canepa, P.; Chabal, Y. J.; Thonhauser, T. Phys. Rev. B: Condens. Matter Mater. Phys. 2013, 87, 094407.

(29) Poloni, R.; Smit, B.; Neaton, J. B. J. Phys. Chem. A 2012, 116, 4957.

(30) Verma, P.; Xu, X.; Truhlar, D. G. J. Phys. Chem. C 2013, 117, 12648.

(31) Perdew, J. P.; Burke, K.; Enzerhof, M. Phys. Rev. Lett. 1996, 77, 3865. Erratum 1997, ibid., 78, 1396.

(32) TURBOMOLE, version 6.4; University of Karlsruhe and Forschungszentrum Karlsruhe GmbH: Karlsruhe, Germany, 2012; http://www.turbomole.com.

(33) Von Arnim, M.; Ahlrichs, R. J. Comput. Chem. 1998, 19, 1746.

(34) Ahlrichs, R. Phys. Chem. Chem. Phys. 2004, 6, 5119.

(35) Eichkorn, K.; Treutler, O.; Öhm, H.; Häser, M.; Ahlrichs, R. Chem. Phys. Lett. 1995, 242, 652.

(36) Eichkorn, K.; Weigend, F.; Treutler, O.; Ahlrichs, R. Theor. Chem. Acc. 1997, 97, 119.

(37) Weigend, F. Phys. Chem. Chem. Phys. 2006, 8, 1057.

(38) Weigend, F.; Ahlrichs, R. Phys. Chem. Chem. Phys. 2005, 7, 3297.

(39) Mitoraj, M.; Michalak, A.; Ziegler, T. J. Chem. Theory Comput. 2009, 5, 962.

(40) te Velde, G.; Bickelhaupt, F. M.; van Gisbergen, S. J. A.; Fonseca Guerra, C.; Baerends, E. J.; Snijders, J. G.; Ziegler, T. J. Comput. Chem. 2001, 22, 931.

(41) Fonseca Guerra, C.; Snijders, J. G.; te Velde, G.; Baerends, E. J. Theor. Chem. Acc. 1998, 99, 391.

(42) ADF2013, SCM, Theoretical Chemistry; Vrije Universiteit: Amsterdam, The Netherlands, http://www.scm.com.

(43) Zhao, Y.; Truhlar, D. G. J. Chem. Phys. 2006, 125, 194101.

(44) Lamberti, C.; Zecchina, A.; Groppo, E.; Bordiga, S. Chem. Soc. Rev. 2010, 39, 4951−5001.

(45) (a) Chavan, S.; Vitillo, J. G.; Groppo, E.; Bonino, F.; Lamberti, C.; Dietzel, P. D. C.; Bordiga, S. J. Phys. Chem. C 2009, 113, 3292−3299. (b) Valenano, L.; Civalleri, B.; Chavan, S.; Palomino, G. T.; Areán, C. O.; Bordiga, S. J. Phys. Chem. C 2010, 114, 11185−11191.

(c) Bordiga, S.; Bonino, F.; Lillerud, K. P.; Lamberti, C. Chem. Soc. Rev. 2010, 39, 4885−4927.

(46) Dewar, M. J. S. Bull. Soc. Chim. Fr. 1951, 18, C79.

(47) Chatt, J.; Duncanson, L. A. J. Chem. Soc. 1953, 2939−2947.

(48) Lupinetti, A. J.; Fau, S.; Frenking, G.; Strauss, S. H. J. Phys. Chem. A 1997, 101, 9551−9559.

(49) Li, P.; Xiang, Y.; Grassian, V. H.; Larsen, S. C. J. Phys. Chem. B 1999, 103, 5058−5062.

(50) Valenzano, L.; Civalleri, B.; Sillar, K.; Sauer, J. J. Phys. Chem. C 2011, 115, 21777−21784.

(51) Valenzano, L.; Vitillo, J. G.; Chavan, S.; Civalleri, B.; Bonino, F.; Bordiga, S.; Lamberti, C. Catal. Today 2012, 182, 67−79.

(52) (a) Reimann, R. H.; Singleton, E. J. Chem. Soc., Dalton Trans. 1973, 2658. (b) Bombin, F.; Carriedo, G. A.; Miguel, J. A.; Riera, V. J. Chem. Soc., Dalton Trans. 1981, 2049.

(53) Bond, A. M.; Colton, R.; McDonald, M. E. Inorg. Chem. 1978, 17, 2842.

(54) (a) Bishop, J. J.; Davison, A. Inorg. Chem. 1971, 10, 832. (b) Pierpont, C. G.; Eisenberg, R. Inorg. Chem. 1972, 11, 828. (c) Saint-Joly, C.; Mari, A.; Gleizes, A.; Dartiguenave, M.; Dartiguenave, Y.; Galy, J. Inorg. Chem. 1980, 19, 2403. (d) Ghilardi, C. A.; Midollini, S.; Sacconi, L. J. Organomet. Chem. 1980, 186, 279− 287. (e) Janikowski, S. K.; Radonovich, L. J.; Groshens, T. J.; Klabunde, K. J. Organometallics 1985, 4, 396. (f) Miedaner, A.; Curtis, C. J.; Wander, S. A.; Goodson, P. A.; DuBois, D. L. Organometallics 1996, 15, 5185. (g) Wilson, A. D.; Fraze, K.; Twamley, B.; Miller, S. M.; DuBois, D. L.; DuBois, M. R. J. Am. Chem. Soc. 2008, 130, 1061.

(55) Krawietz, T. R.; Barich, D. H.; Beck, L. W.; Howard, T.; Xu, T.; Haw, J. F. J. Am. Chem. Soc. 1995, 117, 10407−10408.

(56) Georges, R.; Borras-Almenar, J. J.; Coronado, E.; Curely, J.; Drillon, M. Magnetism: Molecules to Materials I: Models and Experiments; Miller, J. S., Drillon, M.; Wiley-VCH: Weinheim, Germany, 2002.

(57) Kahn, O. Molecular Magnetism; Wiley-VCH: New York, NY, 1993.

(58) Maurice, R.; Verma, P.; Zadrozny, J. M.; Luo, S.; Borycz, J.; Long, J. R.; Truhlar, D. G.; Gagliardi, L. Inorg. Chem. 2013, 52, 9379.

(59) (a) Ray, M.; Golombek, A. P.; Hendrich, M. P.; Young, V. G.; Borovik, A. S. J. Am. Chem. Soc. 1996, 118, 6084−6085. (b) Nguyen, D. H.; Hsu, H.-F.; Millar, M.; Koch, S. A. J. Am. Chem. Soc. 1996, 118, 8963−8964. (c) Davies, S. C.; Hughes, D. L.; Richards, R. L.; Sanders, J. R. Chem. Commun. 1998, 2699−2700.

(60) (a) Yu, D.; Yazaydin, A. O.; Lane, J. R.; Dietzel, P. D. C.; Snurr, R. Q. Chem. Sci. 2013, 4, 3544−3556. (b) Poloni, R.; Lee, K.; Berger, R. F.; Smit, B.; Neaton, J. B. J. Phys. Chem. Lett. 2014, 5, 861.

(61) Farla, J. C. M.; Hendriks, C. A.; Blok, K. Clim. Change 1995, 29, 439−461.

(62) Sato, H.; Kosaka, W.; Matsuda, R.; Hori, A.; Hijikata, Y.; Belosludov, R. V.; Sakaki, S.; Takata, M.; Kitagawa, S. Science 2014, 343, 167−170.

(63) Billy, J.; Fuentes, F.; Sosson, N. US Patent 6,173,585 2001.

(64) Myers, A. L.; Prausnitz, J. M. AIChE J. 1965, 11, 121−127.

(65) Krishna, R.; van Baten, J. M. Phys. Chem. Chem. Phys. 2011, 13, 10593−10616.

(66) Saha, D.; Deng, S. J. Chem. Eng. Data 2009, 54, 2245−2250.